

Light-Induced Magnetization at the Nanoscale

Jonas Wätzel,¹ Primož Rebernik Ribič,² Marcello Coreno,^{2,3} Miltcho B. Danailov,² Christian David,⁴ Alexander Demidovich,² Michele Di Fraia,² Luca Giannessi,^{2,5} Klavs Hansen,⁶ Špela Krušič,⁷ Michele Manfredda,² Michael Meyer,⁸ Andrej Mihelič,⁷ Najmeh Mirian,^{2,9} Oksana Plekan,² Barbara Ressel,¹⁰ Benedikt Rösner,⁴ Alberto Simoncig,² Simone Spampinati,² Matija Stupar,¹⁰ Matjaž Žitnik,⁷ Marco Zangrando,^{2,11} Carlo Callegari,²

Jamal Berakdar,¹ and Giovanni De Ninno^{2,10,*}

¹*Institut für Physik, Martin-Luther-Universität Halle-Wittenberg, 06099 Halle (Saale), Germany*

²*Elettra-Sincrotrone Trieste S.C.p.A., 34149 Trieste, Italy*

³*ISM-CNR, in Basovizza Area Science Park, 34149 Trieste, Italy*

⁴*Paul Scherrer Institut, 5232 Villigen-PSI, Switzerland*

⁵*INFN-LNF, Via E. Fermi 40, 00044 Frascati (Rome), Italy*

⁶*Center for Joint Quantum Studies and Department of Physics, School of Science, Tianjin University, 300072 Tianjin, China*


⁷*J. Stefan Institute, Jamova cesta 39, 1000 Ljubljana, Slovenia*

⁸*European XFEL, Holzkoppel 4, 22869 Schenefeld, Germany*

⁹*Deutsches Elektronen-Synchrotron (DESY), 22607 Hamburg, Germany*

¹⁰*University of Nova Gorica, 5000 Nova Gorica, Slovenia*

¹¹*Istituto Officina dei Materiali, Consiglio Nazionale delle Ricerche, 34149 Trieste, Italy*

 (Received 7 July 2021; revised 19 December 2021; accepted 17 February 2022; published 13 April 2022)

Triggering and switching magnetic moments is of key importance for applications ranging from spintronics to quantum information. A noninvasive ultrafast control at the nanoscale is, however, an open challenge. Here, we propose a novel laser-based scheme for generating atomic-scale charge current loops within femtoseconds. The associated orbital magnetic moments remain ferromagnetically aligned after the laser pulses have ceased and are localized within an area that is tunable via laser parameters and can be chosen to be well below the diffraction limit of the driving laser field. The scheme relies on tuning the phase, polarization, and intensities of two copropagating Gaussian and vortex laser pulses, allowing us to control the spatial extent, direction, and strength of the atomic-scale charge current loops induced in the irradiated sample upon photon absorption. In the experiment we used He atoms driven by an ultraviolet and infrared vortex-beam laser pulses to generate current-carrying Rydberg states and test for the generated magnetic moments via dichroic effects in photoemission. *Ab initio* quantum dynamic simulations and analysis confirm the proposed scenario and provide a quantitative estimate of the generated local moments.

DOI: [10.1103/PhysRevLett.128.157205](https://doi.org/10.1103/PhysRevLett.128.157205)

The spatiotemporal control of the electric component of a laser field opened the door to ultrafast science [1,2]. In the IR, optical, or extreme ultraviolet (XUV) regimes the magnetic field component is of less relevance for applications but for very strong terahertz fields, the magnetic field component may serve to drive the magnetic dynamics, for instance in insulating antiferromagnets [3]. Spin dynamics can also be driven by the electric field of laser pulses by virtue of the spin-orbital coupling and/or transient exchange interactions [4–7]. Local field confinement at surfaces or of arranged plasmonic structures allow for spin excitations [7]. Conventionally, in order to generate magnetic fields for magnetic excitations, charge currents are used, which, however, are difficult to control on the nanometer scale and suffer from joule losses. Here, we propose a method to control laser-generated magnetic moments spatiotemporally and demonstrate the scheme for an atomic gas. All magnetic moments are laser aligned, resulting in a local magnetization

buildup within femtoseconds, which is predicted to persist in the absence of the lasers. The decay of the generated magnetic moments is governed by Rydberg state relaxation, which has been measured and can be in the nanosecond to microsecond regime [8–10].

The basic idea is the following: to bypass the optical diffraction limit on the resolution of the volume in which the magnetic moments are generated, we vary, in a similar way to a stimulated emission depletion (STED) microscope [11], the intensity ratio between the Gaussian XUV pulse and the IR light vortex that trigger the orbital moments. The XUV pulse is tightly focused and copropagates with the IR vortex laser [see Fig. 1(a)]. Both lasers intersect the sample in the same focal plane. The sample, which we magnetize here, is a gas of helium atoms. The IR vortex pulse carries orbital angular momentum (OAM) [12], as well as spin angular momentum (SAM) and has a vanishing intensity in its center, where the XUV intensity peaks. Transferring

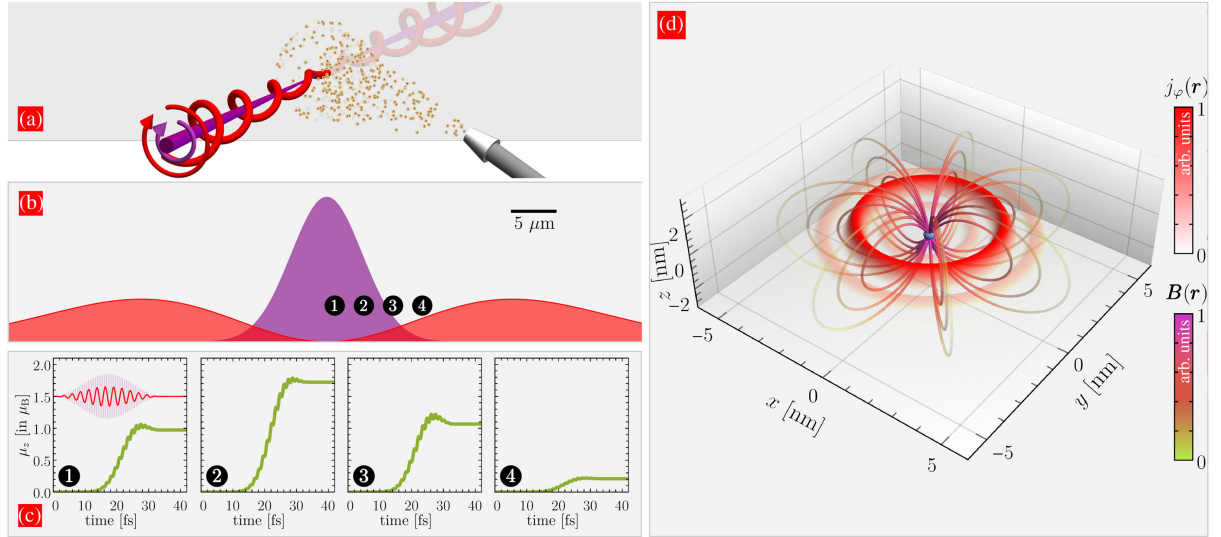


FIG. 1. Experimental setup and temporal buildup of magnetic moments. (a) Sketch of the experimental setup. Collinearly propagating circularly polarized (σ_{XUV}) XUV Gaussian laser pulse (violet) and angular-momentum carrying (with a topological charge m), circularly polarized (σ_{IR}) IR vortex laser pulse (red) intersect a gaseous jet of He atoms traversing the focal plane. (b) Depending on the atom positions in the laser spots (depicted cases are for the following radial distances from the propagation direction: $\rho_1 = 0.4 \mu\text{m}$, $\rho_2 = 2.4 \mu\text{m}$, $\rho_3 = 4.4 \mu\text{m}$, and $\rho_4 = 6.4 \mu\text{m}$), local orbital magnetic moments μ_z are generated in the atom. Theoretical predictions are displayed in (c). The temporal structures of the laser pulses are shown in the inset of (c) (red color indicated the IR vortex pulse, violet color the XUV pulse). (d) shows the quantum mechanically calculated subwavelength confined magnetic field lines for the atom (1) in (b). The total magnetic moment of the excited gas sample as predicted by the theoretical model is $\mu_z = 5.9 \times 10^{-20} \text{ J/T}$ ($6378\mu_B$) for the (low) density of atoms as used in the experiment. All results were obtained for $m = 1 = \sigma_{\text{IR}} = \sigma_{\text{XUV}}$.

optical OAM to electrons is usually highly inefficient (because of the different dispersions) but has been demonstrated experimentally [13,14]. Here, we seek a spatio-temporal control by exciting the ground state to a Rydberg state with one XUV photon. The spatial extent of the Rydberg orbital is thus set by the XUV frequency. Because of its relatively low frequency and intensity, the IR laser affects substantially only the Rydberg states which then attain the well-defined orbital angular momentum $L_z = \langle \Psi | \hat{L}_z | \Psi \rangle$ and carry a unidirectional charge current j_φ , implying an orbital magnetic moment $\mu_z = e/(2m_e)L_z$, where e and m_e are the electron charge and mass. \hat{L} is the orbital angular momentum operator of the parent atom. The direction and amplitude of the current j_φ and the associated magnetic moment μ_z are dictated by the angular momentum of the vortex IR laser, which is parallel to the optical axis. Thus, in contrast to STED [11], our IR pulse does not deplete the intermediate state but it populates the states embodying the nanoscale charge current loop, giving rise to an atomic-size magnetic moment [cf. Fig. (d)].

Our experimental setup depicted in Fig. 1(a) allows for space and time-resolved control on when and where electronic OAM is acquired, and hence j_φ and μ_z are formed: atoms located at the IR laser peak intensity experience effectively a Gaussian-type IR field and a marginal XUV laser intensity [cf. Figs. 1(b) and 1(c)]. Thus, the laser fields have subsidiary influence on these atoms. In contrast, atoms residing around the optical axis, where the XUV (IR)

intensity peaks (diminishes), are excited by the XUV laser in the presence of the IR laser. To generate L_z in the atoms, transfer of optical total angular momentum (TAM) is necessary. For given laser spots, tuning the intensity ratio between the XUV and the IR pulses controls the cross sectional area where the magnetic moments μ_z reside, allowing this way for a nanoscale tuning of the generated magnetic fields with a resolution well below the diffraction limit of the IR laser. The properties of the total magnetic moment depend on the sample atom density. For instance, for a gas target with an areal atom density of $50 \times 10^8 \text{ cm}^{-2}$ only 50 atoms are in a $1 \mu\text{m}^2$ focal plane of the lasers, and the relative interatomic distance is large compared to the size of the atom hosting the Rydberg state. The large distances between the atoms and the energy separation of the Rydberg states from the core states render the charge currents long-lived. The light-induced magnetization follows from a statistical average of the induced atomic magnetic moments μ_z . Full *ab initio* simulations confirm that the maximum μ_z is attained by atoms residing around the radial position 2 in Figs. 1(b) and 1(c). The magnetic field associated with the quantum mechanical j_φ is obtained from classical electrodynamics [results in Fig. 1(d)].

While the atoms are randomly distributed with large relative distances, the spatiotemporal structure of the individual magnetic moments and associated magnetic fields are laser synchronized due to the time and space coherence of the cylindrically symmetric optical fields.

Hence, each atom at a radial distance ρ_a to the optical axis experiences locally and independently the same optical SAM and OAM. Thus, the lasers act as a bias field aligning the magnetic moments ferromagnetically, and in the absence of external magnetic fields, the magnetization is preserved. We note that the induced magnetic field can be broken down to that of one atom, and the extent of the magnetic moment in this atom is tunable by the lasers parameters. Importantly, the induced magnetic moments and associated magnetic fields are robust and do not average to zero over a few optical cycles of the (petahertz) driving lasers. Thus, the associated magnetic fields may sense or affect magnetic dynamics, which proceeds typically in the gigahertz to terahertz frequency range. Generally, driving currents with lasers is achieved based on interference effects between optical excitations [15]. There are theory proposals for petahertz current generation, including the use of structured laser beams [16,17] or plasmonic excitations in metamaterials [18]. Optical rectification [19] or interference of two copropagation beams [20] were studied, as well as intense circularly polarized laser pulses to trigger charge currents [21]. The distinctive feature of our scheme is the all-optical noninvasive (one XUV and one IR photons) generation of nanoscale [Fig. 1(d)] magnetic islands, which are sustainable (duration set by the field-free Rydberg-state relaxation) and controllable in time and direction. In addition, currents with higher multipoles can be generated in atoms in the vicinity of the optical axis [atom at location 1 in Fig. 1(b)], as described in Supplemental Material (SM) [22]. The magnetized atoms are not strongly localized in space [Fig. 1(c)] because of the limited focusing of the XUV laser in our experiment, which has a spot size of $8 \mu\text{m}$ full width at half maximum (FWHM) (more details are in SM [22]). A stronger focusing and/or increased intensity would shrink the effective area where the IR and the XUV laser intersect to generate the magnetic moments.

As a proof of principle, we study a gas of He atoms randomly distributed around the lasers focal point. The XUV laser with photon energy $\hbar\omega_{\text{XUV}} = 23.01 \text{ eV}$ transfers a considerable amount of population from the atomic ground state to the $1s3p$ state, lying 1.58 eV below the first ionization threshold. The moderate intensity IR vortex laser with $\hbar\omega_{\text{IR}} = 1.55 \text{ eV}$ can modify appreciably only the excited state, resulting in a wave packet that circulates unidirectionally around the residual ion and induces a current loop. We confirm this picture by the results of full quantum dynamic simulations, solving numerically the three-dimensional Schrödinger equation in the presence of both laser fields. From the resulting time-dependent wave functions $\Psi(\mathbf{r}, t)$, we infer the time evolution of the atomically localized magnetic moment μ_z . The OAM and SAM of the vortex IR pulse contribute to the TAM, which is necessary for generating the Rydberg loop currents j_φ . More insight is gained from inspecting the interaction $\hat{H}_{\text{int}}^{\text{OV}}$

between the vortex laser field and an atom near the optical axis (i.e., at a small radial distance ρ_a of the atom relative to the IR laser waist w_0), for instance an atom at position 1 in Fig. 1(b). Using cylindrical coordinates, with ρ and φ being the radial and the angular coordinate with respect to the propagation direction (along z), we expand to first order in the small parameter ρ_a/w_0 around the atom position $\mathbf{r}_a = (\rho_a, 0, 0)^T$. For helicity $\sigma = 1$ and for $m \geq 1$, as an example, $\hat{H}_{\text{int}}^{\text{OV}}$ reads (see SM [22])

$$\hat{H}_{\text{int}}^{\text{OV}} \propto \frac{m\alpha_0}{w_0} \left(\frac{\rho_a}{w_0}\right)^{m-1} \hat{q} e^{2i\varphi} + \left(\frac{\rho_a}{w_0}\right)^m \hat{d} e^{i\varphi}. \quad (1)$$

Here, \hat{d} is the (axial-radial) dipole operator, \hat{q} is the (axial-radial) quadrupole operator, and α_0 is a constant depending on the IR focusing conditions [23]. From Eq. (1), which is valid for $\rho_a/w_0 < 1$, we learn that the relative weight of the dipole to quadrupole terms depends on ρ_a for a fixed topological charge m . The intensity ratio between the IR and XUV fields determines the relevant ρ_a , which governs the weight of the multipole contribution, while the topological charge of the optical vortex tunes the multipole character of the generated magnetic moment and the associated magnetic field (see SM [22]). Noting that our induced magnetic moments may persist for nanoseconds, one may probe it using (time-resolved) Kerr spectroscopy [24], neutron scattering [25], or other magnetic field sensors such as nitrogen-vacancy (NV) centers in diamond [26]. We use a method best adapted to our available experimental setup which is dichroism in photoionization. The energy and angle-resolved spectra of the detected photoelectron embody signatures of orbital magnetic moments. For example, Fig. 2(a) shows the photoelectron spectra for an atom near the optical axis [position 1 in Fig. 1(b)], which has been magnetized by one XUV and one IR photon and then the current-carrying state is ionized by one IR photon [see inset of Fig. 2(c)]. The spectra of the resulting photoelectron are used to characterize μ_z . We compare cases for an IR photon with TAM = $+2\hbar$ (black curves) or TAM = $-2\hbar$ (red curves). The photoelectron peaks (sidebands, SB) are separated by the IR photon energy. The energy and angle-resolved differential cross sections $w_{\text{TAM}}(E_k, \vartheta_k)$ for the emission of electrons with energy E_k along a direction ϑ_k , depend on TAM. Thus, we can introduce the dichroism (blue curve)

$$D = \frac{w_+(E_k, \vartheta_k) - w_-(E_k, \vartheta_k)}{w_+(E_k, \vartheta_k) + w_-(E_k, \vartheta_k)}, \quad (2)$$

where \pm subscripts refer to TAM signs. D changes sign when switching the observation angle from parallel ($\vartheta_k = 0$) to perpendicular ($\vartheta_k = \pi/2$) emission with respect to the laser propagation axis. The characteristic angular dependence of the dichroism is related to the photoexcited magnetic moment μ . Absorption of one IR photon with

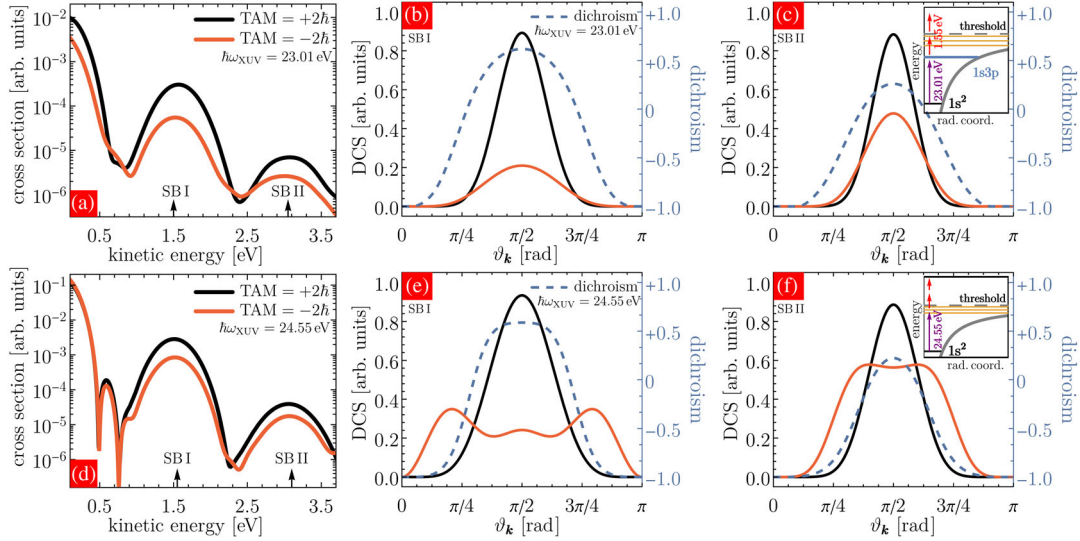


FIG. 2. Theoretical prediction of photoionization of an atom close to the vortex optical axis which serves as a measurement instrument for the photoexcited magnetic moments. Theory results for the angle-integrated energy spectra (a),(d), and angular-resolved differential cross section (b),(c),(e),(f) for photoelectrons originating from the XUV-IR laser-prepared rotating electronic wave packet of one atom located near the optical axis [position 1 in Fig. 1(b)]. The laser frequencies are chosen such that the wave packet, upon absorption of *one* IR vortex photon, is generated slightly below (upper row) or above (lower row) the single ionization threshold. Insets indicate excitation scheme. Red (violet) arrows stand for IR (XUV) photon absorption. The IR optical vortex has total angular momentum (TAM) of either $-2\hbar$ or $+2\hbar$. The dichroism is plotted with dashed blue lines.

TAM = $+2\hbar$ by an atom in the intermediate state $1s3p$ leads to a quantum state with a (normalized) magnetic moment μ_+ [cf. Eq. (1)]. This is because the XUV photon is circularly polarized and the angular momentum of the intermediate state adds up to the IR photon TAM when creating the rotating Rydberg state. Analytical considerations supported by full numerical simulations evidence that the electron charge density associated with μ_+ accumulates perpendicular to the light field's propagation axis. Changing now the sign of the photonic TAM excites the atom to a different quantum state with a magnetic moment μ_- that has an opposite sign to μ_+ . As a result, we expect a reduced charge density accumulation in the perpendicular plane, which is evidenced by the DCS of the emitted photoelectron (more details in SM [22]). It is this distinctive behavior of μ_+ and μ_- which causes the change in sign of the resulting dichroism D . Importantly, the energy and angular positions of the zeros in D depend on the presence or absence of nondipolar contributions (see SM [22]).

The findings regarding μ_+ and μ_- are valid for IR-excited states slightly below or above the single ionization threshold, as demonstrated by Fig. 2. In the latter case, the charge looping unfolds simultaneously with the fragmentation resulting in a time-dependent μ_+ and μ_- , or in other words, a photoelectron experiences a magnetic torque pulse with a duration depending on the photoelectron energy. Since μ_+ and μ_- is localized within the range where the atomic potential varies significantly, its duration can be tuned by changing the IR frequency, which modifies the photoelectron energy. A typical case is depicted in Figs. 2(d)–2(f) for

an atom at the position 1 in Fig. 1(b). The XUV photon energy is now adjusted to $\hbar\omega_{\text{XUV}} = 24.55$ eV, meaning that a Rydberg manifold is first populated by the XUV photon absorption. The IR optical vortex acts once the Rydberg state is populated, generating a rotating *and* receding (photo) electron wave packet.

To prove the theoretical predictions, we performed an experiment corresponding to the scheme depicted in the inset of Fig. 2(f), where the central photon energy of the XUV laser field is 24.55 eV. Similar to Figs. 2(d)–2(f), we measured the DCS of the photoelectrons, deduced the dichroism D , and compared it with the theory. The XUV laser pulse stems from the FERMI FEL [27,28] source, and it is focused down to a Gaussian-shaped spot with a full width at half maximum (FWHM) of eight microns. The effective interaction region where the FEL pulse and the IR vortex intensity profiles (FWHM is 50 μm) intersect is restricted to the vicinity of the optical axis, i.e., the condition for the theoretical model $\rho_d/w_0 < 1$ is fulfilled. We performed two sets of measurements. In the first set, the IR laser pulse was a Gaussian-shaped circularly polarized laser pulse giving rise to circular dichroism [29,30] only (photon OAM is zero). The DCSs for the first and second sidebands for this case are shown in Figs. 3(a) and 3(f) and compared to the theory. The measured circular dichroism D_c distributions are shown in Figs. 3(c) and 3(h), showing a good agreement with the theory and are in line with existing literature [29–31]. In the second set, we substitute the unstructured IR fields with vortex fields carrying the same SAM as in the first set of measurements but also one quantum of OAM, allowing

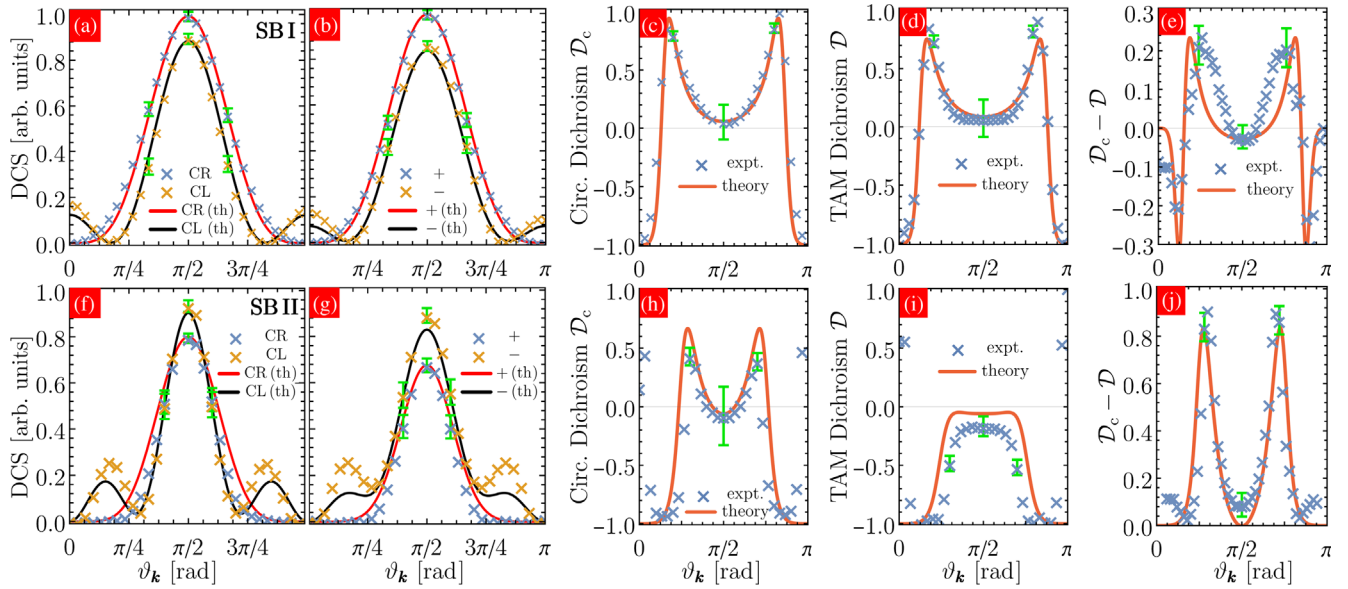


FIG. 3. Experimental vs theoretical photoelectron spectra and DCSs for different combinations of IR spin and OAM. Experimental verification of angular momentum transfers in first and second sidebands (SB) (upper row SB I, lower row SB II). The first two panels from the left show the individual DCS when the IR field does not carry OAM and is left (CL) or right (CR) circularly polarized (a),(f). Panels (b),(g) correspond to an IR vortex carrying TAM = $\pm 2\hbar$. From the measurement we infer the dichroism distributions: circular (c),(h) and TAM dichroism (d),(i). The outer right panels (e),(j) show the difference between both dichroism types. For a discussion on the evaluation of experimental error bars, see SM [22].

tuning to TAM = $\pm 2\hbar$. The corresponding results are presented in Figs. 3(b) and 3(g). The dominance of the SAM transfer via dipole transitions is evident when comparing to the first set of measurements. Investigating the corresponding TAM dichroism D , shown in Figs. 3(d) and 3(i), reveals for the first sideband a small deviation from the circular dichroism, although the general curves' shapes are very similar. The deviation becomes more prominent for the second sideband (when two IR photons are involved). An important quantity is the difference between both dichroism types, i.e., $D_c - D$ as presented in Figs. 3(e) and 3(j). The overall good agreement between the experiment and the theory endorses our underlying picture about the generation of μ . The remaining differences between the theory and the experiment are traced back to nondipolar interactions, see Eq. (1), resulting in moderate changes in the angular dependence of D . For the first sideband, the nodes of the OAM-affected dichroism D [Fig. 3(d)] are slightly shifted toward the propagation axis (toward $\vartheta_k = 0$) in comparison to D_c , which yields the observed shape and change of signs of $D_c - D$. At $\vartheta_k = 0$ and $\vartheta_k = \pi/2$ the difference is practically zero. For the second sideband, the general difference is even more pronounced but shows a similar magnitude. Generally, we attribute the difference in the dichroism types to traces of OAM transfer (to the photoelectrons) for both sidebands, which survived the averaging over the randomly distributed atoms from which the photoelectron signals stem.

Our theory and experiments demonstrate how to laser generate nanoscale ferromagnetically aligned magnetic moments and show how to control their characteristics.

The agreement of the results of our *ab initio* modeling with the experimental data supports the validity of the general scheme. In particular, it confirms the femtosecond buildup of atomically confined directed current densities leading to the formation of nanometer scale magnetization that lasts for nanoseconds. At atomic position “2” (see Fig. 1, where the photoinduced magnetic moment is $\sim 1.5 \mu_B$) we estimate an on-axis magnetic field ~ 0.1 mT which can be used for small-amplitude transversal spin excitations [32]. While He atoms can be handled well both theoretically and experimentally and hence are ideal for a proof-of-principle study, our scheme is not restricted to He. Rydberg states are a generic feature of electronic compounds, and their photoexcitation does not require a symmetry breaking in the sample. For example, the approach can be applied to adsorbates such as rare gases that are physisorbed at magnetically active surfaces [33], allowing us to study the spatiotemporal material's magnetic response to the fields of the photogenerated magnetic moments.

We acknowledge the support of the project “Triggering forbidden phenomena with twisted light and particle beams” (No. J1-8134) and “Structured light as a tool for triggering and probing new states of matter” (No. J1-3012), funded by the Slovenian Research Agency (ARRS), and of the EU-H2020 project NFFA (Grant No. 654360). Theoretical study has been financed by the German Science Foundation (DFG), within the priority program 1840 “Quantum dynamics in tailored intense fields,” SFB-TRR227, and WA 4352/2-1. We thank R. Dörner for important comments and advice.

- * giovanni.deninno@elettra.eu
- [1] F. Krausz and M. Ivanov, Attosecond physics, *Rev. Mod. Phys.* **81**, 163 (2009).
- [2] H. Rubinsztein-Dunlop *et al.*, Roadmap on structured light, *J. Opt.* **19**, 013001 (2017).
- [3] T. Kampfrath, A. Sell, G. Klatt, A. Pashkin, S. Mährlein, T. Dekorsy, M. Wolf, M. Fiebig, A. Leitenstorfer, and R. Huber, Coherent terahertz control of antiferromagnetic spin waves, *Nat. Photonics* **5**, 31 (2011).
- [4] M. Finazzi, M. Savoini, A. R. Khorsand, A. Tsukamoto, A. Itoh, L. Duò, A. Kirilyuk, Th. Rasing, and M. Ezawa, Laser-Induced Magnetic Nanostructures with Tunable Topological Properties, *Phys. Rev. Lett.* **110**, 177205 (2013).
- [5] L. Le Guyader, M. Savoini, S. El Moussaoui, M. Buzzi, A. Tsukamoto, A. Itoh, A. Kirilyuk, T. Rasing, A. V. Kimel, and F. Nolting, Nanoscale sub-100 picosecond all-optical magnetization switching in GdFeCo microstructures, *Nat. Commun.* **6**, 5839 (2015).
- [6] N. Maccaferri, I. Zubritskaya, I. Rzdolski, I. Chioar, V. Belotelov, V. Kapaklis, P. M. Oppeneer, and A. Dmitriev, Nanoscale magnetophotonics, *J. Appl. Phys.* **127**, 080903 (2020).
- [7] J. R. Hortensius, D. Afanasiev, M. Matthiesen, R. Leenders, R. Citro, A. V. Kimel, R. V. Mikhaylovskiy, B. A. Ivanov, and A. D. Caviglia, Coherent spin-wave transport in an antiferromagnet, *Nat. Phys.* **17**, 1001 (2021).
- [8] B. Butscher, J. Nipper, J. B. Balewski, L. Kukota, V. Bendkowsky, R. Löw, and T. Pfau, Atom-molecule coherence for ultralong-range Rydberg dimers, *Nat. Phys.* **6**, 970 (2010).
- [9] D. B. Branden, T. Juhasz, T. Mahlokozera, C. Vesa, R. O. Wilson, M. Zheng, A. Kortyna, and D. A. Tate, Radiative lifetime measurements of rubidium Rydberg states, *J. Phys. B* **43**, 015002 (2010).
- [10] M. Mack, J. Grimm, F. Karlewski, Lórinç Sárkány, H. Hattermann, and J. Fortágh, All-optical measurement of Rydberg-state lifetimes, *Phys. Rev. A* **92**, 012517 (2015).
- [11] T. A. Klar and S. W. Hell, Subdiffraction resolution in far-field fluorescence microscopy, *Opt. Lett.* **24**, 954 (1999).
- [12] L. Allen, M. W. Beijersbergen, R. J. C. Spreeuw, and J. P. Woerdman, Angular momentum of light and the transformation of Laguerre-Gaussian laser modes, *Phys. Rev. A* **45**, 8185 (1992).
- [13] C. T. Schmiegelow, J. Schulz, H. Kaufmann, T. Ruster, U. G. Poschinger, and F. Schmidt-Kaler, Transfer of optical orbital angular momentum to a bound electron, *Nat. Commun.* **7**, 12998 (2016).
- [14] G. De Ninno *et al.*, Photoelectric effect with a twist, *Nat. Photonics* **14**, 554 (2020).
- [15] S. Sederberg, F. Kong, F. Hufnagel, C. Zhang, E. Karimi, and P. B. Corkum, Vectorized optoelectronic control and metrology in a semiconductor, *Nat. Photonics* **14**, 680 (2020).
- [16] C. Guclu, M. Veysi, and F. Capolino, Photoinduced magnetic nanoprobe excited by an azimuthally polarized vector beam, *ACS Photonics* **3**, 2049 (2016).
- [17] J. Wätzel, C. Granados, and J. Berakdar, Magnetoelectric response of quantum structures driven by vector beams, *Phys. Rev. B* **99**, 085425 (2019).
- [18] S. Campione, C. Guclu, R. Ragan, and F. Capolino, Enhanced magnetic and electric fields via fano resonances in metasurfaces of circular clusters of plasmonic nanoparticles, *ACS Photonics* **1**, 254 (2014).
- [19] T. Bose and J. Berakdar, Nonlinear magneto-optical response to light carrying orbital angular momentum, *J. Opt.* **16**, 125201 (2014).
- [20] Y. Shi, J. Vieira, R. M. G. M. Trines, R. Bingham, B. F. Shen, and R. J. Kingham, Magnetic Field Generation in Plasma Waves Driven by Co-Propagating Intense Twisted Lasers, *Phys. Rev. Lett.* **121**, 145002 (2018).
- [21] S. Eckart *et al.*, Ultrafast preparation and detection of ring currents in single atoms, *Nat. Phys.* **14**, 701 (2018).
- [22] See Supplemental Material at <http://link.aps.org/supplemental/10.1103/PhysRevLett.128.157205> for more details on the theoretical model, numerical implementation and experiment.
- [23] J. Wätzel and J. Berakdar, Electrons in intense laser with local phase, polarization, and skyrmionic textures, *Phys. Rev. A* **102**, 063105 (2020).
- [24] I. Rzdolski, A. Alekhin, U. Martens, D. Bürstel, D. Diesing, M. Münzenberg, U. Bovensiepen, and A. Melnikov, Analysis of the time-resolved magneto-optical Kerr effect for ultrafast magnetization dynamics in ferromagnetic thin films, *J. Phys. Condens. Matter* **29**, 174002 (2017).
- [25] S. T. Bramwell and B. Keimer, Neutron scattering from quantum condensed matter, *Nat. Mater.* **13**, 763 (2014).
- [26] M. W. Doherty, N. B. Manson, P. Delaney, F. Jelezko, J. Wrachtrup, and L. C. Hollenberg, The nitrogen-vacancy colour centre in diamond, *Phys. Rep.* **528**, 1 (2013).
- [27] M. Meyer, J. T. Costello, S. Düsterer, W. B. Li, and P. Radcliffe, Two-colour experiments in the gas phase, *J. Phys. B* **43**, 194006 (2010).
- [28] E. Allaria *et al.*, Highly Coherent and Stable Pulses from the FERMI Seeded Free-Electron Laser in the Extreme Ultraviolet, *Nat. Photonics* **6**, 699 (2012).
- [29] T. Mazza *et al.*, Determining the polarization state of an extreme ultraviolet free-electron laser beam using atomic circular dichroism, *Nat. Commun.* **5**, 3648 (2014).
- [30] A. K. Kazansky, A. V. Grigorieva, and N. M. Kabachnik, Circular Dichroism in Laser-Assisted Short-Pulse Photoionization, *Phys. Rev. Lett.* **107**, 253002 (2011).
- [31] T. Mazza *et al.*, Angular distribution and circular dichroism in the two-colour XUV + NIR above-threshold ionization of helium, *J. Mod. Opt.* **63**, 367 (2016).
- [32] A. F. Schäffer, J. Wätzel, and J. Berakdar, Spatio-temporal tracking of magnetic dynamics of adatoms via magnetic fields driven by femtosecond optical vortices, *Proc. SPIE Int. Soc. Opt. Eng.* **9931**, 99311B (2016).
- [33] K. Jacobi, Ya-po. Hsu, and H. H. Rotermund, Photoemission from Ne, Ar, Kr and Xe layers on Ni(110) and Ga films, *Surf. Sci.* **114**, 683 (1982).